

Journal of Biomedical Optics

BiomedicalOptics.SPIEDigitalLibrary.org

Grueneisen relaxation photoacoustic microscopy *in vivo*

Jun Ma
Junhui Shi
Pengfei Hai
Yong Zhou
Lihong V. Wang

SPIE.

Jun Ma, Junhui Shi, Pengfei Hai, Yong Zhou, Lihong V. Wang, "Grueneisen relaxation photoacoustic microscopy *in vivo*," *J. Biomed. Opt.* **21**(6), 066005 (2016), doi: 10.1117/1.JBO.21.6.066005.

Grueneisen relaxation photoacoustic microscopy *in vivo*

Jun Ma, Junhui Shi, Pengfei Hai, Yong Zhou, and Lihong V. Wang*

Washington University in St. Louis, Department of Biomedical Engineering, Optical Imaging Laboratory, Campus Box 1097, One Brooking Drive, St. Louis, Missouri 63130-4899, United States

Abstract. Grueneisen relaxation photoacoustic microscopy (GR-PAM) can achieve optically defined axial resolution, but it has been limited to *ex vivo* demonstrations so far. Here, we present the first *in vivo* image of a mouse brain acquired with GR-PAM. To induce the GR effect, an intensity-modulated continuous-wave laser was employed to heat absorbing objects. In phantom experiments, an axial resolution of 12.5 μm was achieved, which is sixfold better than the value achieved by conventional optical-resolution PAM. This axial-resolution improvement was further demonstrated by imaging a mouse brain *in vivo*, where significantly narrower axial profiles of blood vessels were observed. The *in vivo* demonstration of GR-PAM shows the potential of this modality for label-free and high-resolution anatomical and functional imaging of biological tissues. © 2016 Society of Photo-Optical Instrumentation Engineers (SPIE) [DOI: 10.1117/1.JBO.21.6.066005]

Keywords: photoacoustic imaging; nonlinear microscopy; Grueneisen relaxation; optical sectioning.

Paper 160121RR received Feb. 26, 2016; accepted for publication May 19, 2016; published online Jun. 8, 2016.

1 Introduction

Photoacoustic microscopy (PAM), based on the photoacoustic effect, is a hybrid imaging modality that acoustically detects the optical absorption contrast in biological tissues.¹ PAM can provide both anatomical and functional information about biological systems by probing a wide variety of endogenous contrast agents, such as hemoglobin, melanin, DNA/RNA, and lipids.²⁻⁷ With tightly focused light, PAM can achieve optical diffraction-limited lateral resolutions down to the submicron scale.² This optical-resolution PAM (OR-PAM) enables *in vivo* functional imaging of blood vessels down to the capillary level. However, the axial resolution of conventional OR-PAM, which is determined by the frequency bandwidth of the detectable ultrasonic signal from a targeted depth in tissue and the speed of sound (SOS), is typically one order of magnitude worse than its lateral resolution.⁸ Increasing the frequency bandwidth of the ultrasonic transducer (UT) can improve the axial resolution in conventional OR-PAM, at the expense of tissue attenuation of high-frequency photoacoustic (PA) signals.^{9,10} Reducing the SOS can also improve the axial resolution but often necessitates disturbing the original biological environment.¹¹ In addition, a multiview OR-PAM, which images the sample from multiple view angles and then reconstructs the image with a multiview deconvolution method, has been proposed to realize three-dimensional (3-D) optical resolution.¹² However, it was demonstrated only in (semi-)transparent samples, such as zebra fish.

Micron and submicron axial resolutions have been achieved in OR-PAM by exploiting several nonlinear effects, such as transient absorption,¹³ photobleaching,¹⁴ and Grueneisen relaxation (GR).¹⁵ However, all of these nonlinear effects have been limited to *ex vivo* imaging of red blood cells, and no *in vivo* imaging has been demonstrated thus far, despite its importance in biomedical studies.

In this paper, we demonstrate *in vivo* GR-PAM. To generate the GR effect, an intensity-modulated continuous-wave (CW) laser was used to heat absorbing objects. With its optical-sectioning capability, GR-PAM demonstrated an axial resolution of $\sim 12.5 \mu\text{m}$, which is determined by the depth of focus of the laser beam. This axial-resolution improvement was first demonstrated by imaging a human hair phantom and then by imaging bovine blood in a plastic tube. The blurring of the hair and the tube along the axial direction in the PA images were significantly diminished. We then applied GR-PAM to image mouse brains *in vivo* and observed narrower axial profiles of blood vessels. This *in vivo* demonstration of GR-PAM shows its potential for label-free and high-resolution anatomical and functional imaging of biological tissues.

2 Methods

GR-PAM relies on the nonlinear GR effect, which describes the Grueneisen parameter change induced by heating absorbers with light emitted from a pulsed laser or an intensity-modulated CW laser.^{15,16} As the temperature rises, the Grueneisen parameter, which exhibits an approximate linear dependence on the temperature, increases and results in a stronger PA signal.¹⁷ The original experimental process to obtain PA signals with the GR effect was fully described in our previous study.¹⁵ Briefly, two identical laser pulses are delivered to absorbers sequentially with a submicrosecond delay. The first laser pulse generates a PA signal and simultaneously heats the absorber. Within the thermal relaxation time of the first pulse excitation out of the voxel, the second laser pulse excites the heated absorber, which generates a stronger PA signal than the first, based on the GR effect.

For the first laser pulse, with an optical fluence of $F_1(x, y)$, the generated initial pressure rise $p_1(x, y)$ can be expressed as

*Address all correspondence to: Lihong V. Wang, E-mail: lhwang@wustl.edu

$$p_1(x, y) = \Gamma_0 \eta_{th} \mu_a(x, y) F_1(x, y), \quad (1)$$

where Γ_0 is the Grueneisen parameter at the initial temperature and depends on the local temperature of the absorber, η_{th} is the heat conversion efficiency, and $\mu_a(x, y)$ is the optical absorption coefficient. Within the thermal relaxation time of the heating from the first laser pulse, the second laser pulse, with an optical fluence of $F_2(x, y)$, generates another initial pressure rise $p_2(x, y)$:

$$p_2(x, y) = [\Gamma_0 + G \eta_{th} \mu_a(x, y) F_1(x, y)] \eta_{th} \mu_a(x, y) F_2(x, y), \quad (2)$$

where G is a coefficient that relates the change of the Grueneisen parameter to the absorbed energy from the first laser pulse. The GR-PAM signal $\Delta p(x, y)$ is obtained by subtracting $p_1(x, y)$ from $p_2(x, y)$. If two identical laser pulses [$F_1(x, y) = F_2(x, y) = F(x, y)$] and a planar target with uniform $\mu_a(x, y)$ [$\mu_a(x, y) = \mu_a$] are considered, the GR-PAM signal $\Delta p(x, y)$ can be written as

$$\Delta p(x, y) = p_2(x, y) - p_1(x, y) = G \eta_{th}^2 \mu_a^2 F(x, y)^2, \quad (3)$$

which shows a quadratic dependence on the optical fluence of the laser pulse. This nonlinear relationship, analogous to other nonlinear microscopies, such as two-photon fluorescent microscopy¹⁸ and two-photon absorption-induced PAM,^{19,20} can significantly improve the axial resolution of GR-PAM. In this work, an intensity-modulated CW laser, instead of a nano-second pulsed laser as in Ref. 13, was used for heating absorbers because the CW laser is much less expensive.

3 Experimental Setup

Figure 1(a) shows a schematic of the GR-PAM system. Light from a diode-pumped solid-state pulsed laser (532 nm, 10-ns pulse duration, Innoslab BX2II-E, Edgewave) and a CW laser (532 nm, MLL-III-532, Changchun New Industries) is combined and focused by an objective lens with a numerical aperture (NA) of 0.3. The light, with a focal spot diameter of $\sim 1 \mu\text{m}$, is then delivered to the sample. Light beams from the two lasers are adjusted to be confocal for generating the maximum nonlinear PA signals. The intensity of the light from the pulsed laser is monitored with a photodiode (SM05PD1A, Thorlabs) to compensate for intensity fluctuations. Figure 1(b) shows the time sequence of the pulsed laser, CW laser, and PA signals.

The pulsed laser generates a 1-kHz-repetition-rate dual-pulse train. In each train, the first pulse is triggered to generate a baseline PA signal before the CW laser heating [PA1 in Fig. 1(b)]. The second pulse is triggered at the end of the CW laser heating to create a stronger PA signal induced by the GR effect [PA2 in Fig. 1(b)]. The time interval between the two pulses is $\sim 100 \mu\text{s}$. The CW laser, which serves as the heating source, is intensity modulated with a frequency of 1 kHz and has an illumination duration of 30 μs . Since the estimated thermal relaxation time for a 1- μm diameter optical heating spot is much less than the 1-ms period of the CW laser,²¹ the thermal heating generated by the CW laser in each period can dissipate with negligible influence on the next period. The generated PA signals are detected by a focused UT (V324SU, Olympus) with a central frequency of 25 MHz and then amplified by ~ 50 dB (ZFL-500LN+, Minicircuits). The amplified signals are collected by a data acquisition (DAQ) unit with a sampling rate of 500 MHz (ATS9350, AlazarTech). As shown in Fig. 1(a), the UT is placed at the side of the sample, orthogonal to the direction of light delivery. This orthogonal configuration needs no complicated prism and lens for acoustic-optical coaxial alignment.²² To maximize PA signals, the acoustic focus is adjusted to be confocal to the light focus. During imaging, both the laser light and the UT are kept static, and only the sample is scanned in 3-D with a three-axis motor stage (PLS-85, PI miCos). At each imaging position, the difference between the peak-to-peak values of the two PA signals [PA1 and PA2 in Fig. 1(b)] is extracted as the GR-PAM signal for image reconstruction. It should be pointed out that 3-D scanning instead of 2-D scanning is needed for the GR-PAM to acquire a 3-D image, because only the peak-to-peak value of the time-resolved PA signal at each focal position is extracted for image reconstruction. The 3-D image from conventional OR-PAM is also acquired by 3-D scanning to avoid optical defocusing, with the peak-to-peak value of the time-resolved PA signal from the first laser pulse (PA1) used for image reconstruction. In the rest of this paper, this method is referred to as 3-D-scanning conventional OR-PAM. Currently, the imaging speed of GR-PAM is limited by the laser repetition rate of 1 kHz. For a volume of $200 \times 200 \times 100$ pixels, the imaging time for GR-PAM is 2.2 h. The imaging speed can be greatly improved by using a laser with higher repetition rate.

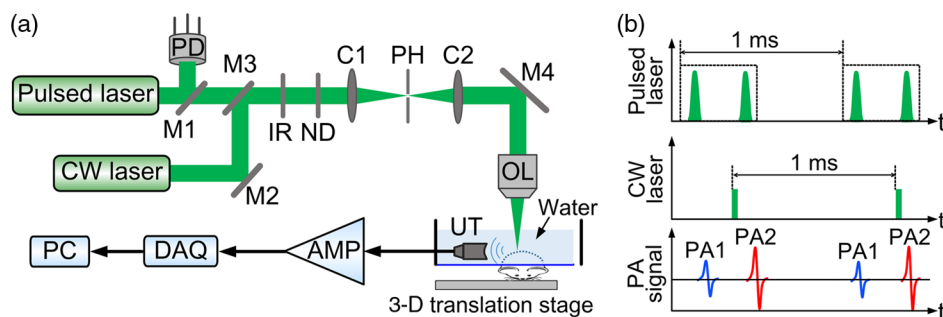


Fig. 1 (a) Schematic of the experimental setup of the GR-PAM system. AMP, amplifier; C1 and C2, condenser lenses; CW laser, continuous-wave laser; DAQ, data acquisition unit; IR, iris; M1, M2, M3, and M4, mirrors; ND, neutral density filter; OL, objective lens; PC, computer; PD, photodiode; PH, pinhole; UT, ultrasonic transducer; 3-D, three-dimension. (b) Diagram of the time sequence of the pulsed laser, CW laser, and PA signals.

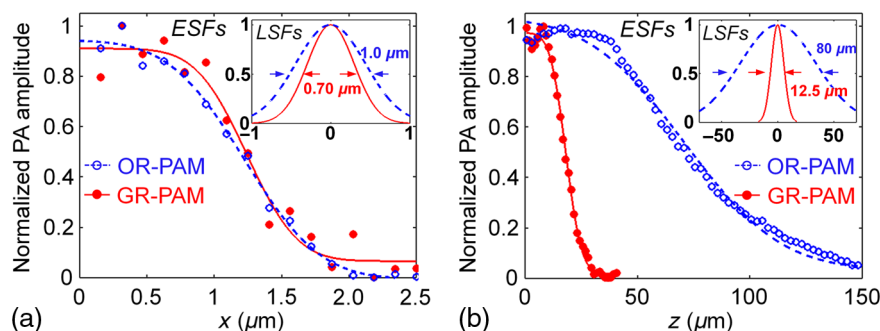


Fig. 2 (a) Lateral profiles of a sharp metal edge measured by GR-PAM and 3-D-scanning conventional optical-resolution microscopy (OR-PAM). The values of FWHM of the profiles from GR-PAM and 3-D-scanning conventional OR-PAM are ~ 0.7 and $1.0 \mu\text{m}$, respectively. (b) Axial profiles of a thin layer of ink acquired by GR-PAM and 3-D-scanning conventional OR-PAM. The FWHMs of the profiles from GR-PAM and 3-D-scanning conventional OR-PAM are 12.5 and $80 \mu\text{m}$, respectively. ESFs, edge spread functions; LSFs, line spread functions.

4 Results

As mentioned previously, the resolution improvement in GR-PAM results from the quadratic dependence of PA signals on the incident optical fluence. The lateral resolution was measured by scanning across a sharp metal edge. Figure 2(a) shows the edge spread functions (ESFs) of GR-PAM and 3-D-scanning conventional OR-PAM. For 3-D-scanning conventional OR-PAM, the ESF was calculated directly from the PA signal generated by the first excitation pulse without CW laser heating [PA1 in Fig. 1(b)]. The line spread function (LSF) was then obtained from the derivation of the ESF. The lateral resolution was qualified by the full width at half maximum (FWHM) value of the LSF [inset of Fig. 2(a)]. GR-PAM has a lateral resolution of $0.7 \mu\text{m}$, which is ~ 1.4 times better than the value of $1.0 \mu\text{m}$ for 3-D-scanning conventional OR-PAM, and is close to the theoretical improvement factor of $\sqrt{2}$.¹⁵ The axial resolution of GR-PAM was quantified by imaging a thin layer of black

ink coated on a cover glass. From the LSFs, the measured axial resolution of GR-PAM was $\sim 12.5 \mu\text{m}$, which is close to the theoretical value of $10.6 \mu\text{m}$ estimated from the optical depth of the focus (L_d) given by $L_d = 1.8 \lambda_o / \text{NA}^2$, where λ_o is the laser wavelength and NA is the numerical aperture of the objective.¹⁵ This value is ~ 6.4 times better than that measured by 3-D-scanning conventional OR-PAM ($\sim 80 \mu\text{m}$), as plotted in Fig. 2(b).

The optically defined axial resolution of GR-PAM was demonstrated by imaging a human hair phantom. Figures 3(a) and 3(b) are images of the phantom captured by GR-PAM and 3-D-scanning conventional OR-PAM, respectively. Two hairs of the phantom were imaged, one along the y -axis and the other in the x - z plane crossing atop the first one, as illustrated by the dashed box in Fig. 3(e). The hair image from 3-D-scanning conventional OR-PAM is severely blurred due to the inferior acoustically determined axial resolution. Figures 3(c) and 3(d) show,

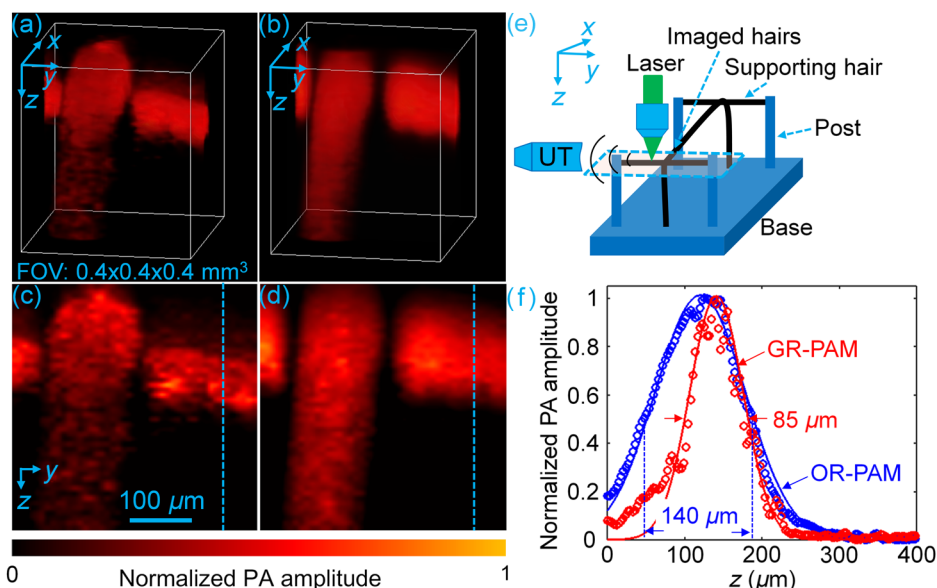


Fig. 3 (a) 3-D volume-rendered PA images of a hair phantom from GR-PAM and (b) 3-D-scanning conventional OR-PAM. FOV, field of view. (c) Schematic configuration of the hair phantom experiment. The dashed box indicates the imaged area of the phantom. UT, ultrasonic transducer. (d) and (e) are MAP images along the x -axis of the volume-rendered PA images in (a) and (b), respectively. (f) Profiles of the hair along the dashed lines in (d) and (e).

respectively, the maximum amplitude projection (MAP) images along the x -axis of the volume-rendered PA images in Figs. 3(a) and 3(b). The profiles of the hairs along the dashed lines in Figs. 3(c) and 3(d) are plotted in Fig. 3(f). The diameter of the hair measured by 3-D-scanning conventional OR-PAM was $\sim 140 \mu\text{m}$. In contrast, the diameter of the same hair measured by GR-PAM was $\sim 85 \mu\text{m}$, which is much closer to the value of $84 \mu\text{m}$ measured by an optical microscope. As a result, the measured diameter of the hair structure along the z -axis is significantly reduced in GR-PAM, owing to its optical-sectioning capability.

To mimic blood vessels, we imaged bovine blood in a plastic tube with an inner diameter of $100 \mu\text{m}$. Figures 4(a) and 4(b) show 3-D images of the tube acquired by GR-PAM and 3-D-scanning conventional OR-PAM, respectively. The shadow of the tube along the z -axis is reduced, similar to the situation for the previous hair phantom. Figures 4(c) and 4(d) show B-scan images of the tube in the x - z plane at the position y_0 , as indicated in Figs. 4(a) and 4(b), respectively. By plotting the profiles along the z -axis at the position denoted by the dashed line in Figs. 4(c) and 4(d), the fitted diameter from GR-PAM, as shown in Fig. 4(e), is $\sim 107 \mu\text{m}$. This value is much closer to the actual value of $\sim 100 \mu\text{m}$ than the diameter of $\sim 160 \mu\text{m}$ from 3-D-scanning conventional OR-PAM.

We then imaged the brain of a female ND4 Swiss Webster mouse (Harlan Laboratory Inc., Indianapolis) *in vivo*. All procedures for the animal experiment were carried out in

accordance with the laboratory animal protocol approved by the Animal Studies Committee at Washington University in St. Louis. The mouse scalp was removed but the skull was kept intact. During the experiment, the pulse energy from the pulsed laser was $0.5 \mu\text{J}$, and the average power for the modulated CW laser was 20 mW. For the modulated CW light with a duration of $30 \mu\text{s}$, the energy delivered within each modulation period was $\sim 0.6 \mu\text{J}$. Below the skull with a thickness of $\sim 150 \mu\text{m}$,²³ the combined optical fluence of the pulsed and CW laser on the brain surface was $\sim 16 \text{mJ}/\text{cm}^2$, which is within the American National Standards Institute (ANSI) safety limit ($20 \text{mJ}/\text{cm}^2$). For this optical fluence, the maximum amplitude of the PA signal with laser heating (PA2) was about 10% greater than the PA signal (PA1) without heating at the same position, which corresponds to a temperature increase of 3°C .¹⁶ Figures 5(a) and 5(b) show the mouse brain images from GR-PAM and 3-D-scanning conventional OR-PAM, respectively. Because GR-PAM reconstructs the image from the difference of PA signals generated with and without CW laser heating, the signal-to-noise ratio of GR-PAM is nearly 4 times lower than that of 3-D-scanning conventional OR-PAM. Thus, the image contrast-to-noise ratio of GR-PAM is generally inferior to that of 3-D-scanning conventional OR-PAM, as shown in Fig. 5(b). Figures 5(c) and 5(d), respectively, show the GR-PAM and 3-D-scanning conventional OR-PAM images obtained by averaging five adjacent B-scan images at the location indicated by the dashed lines. From the profiles along the dashed lines in

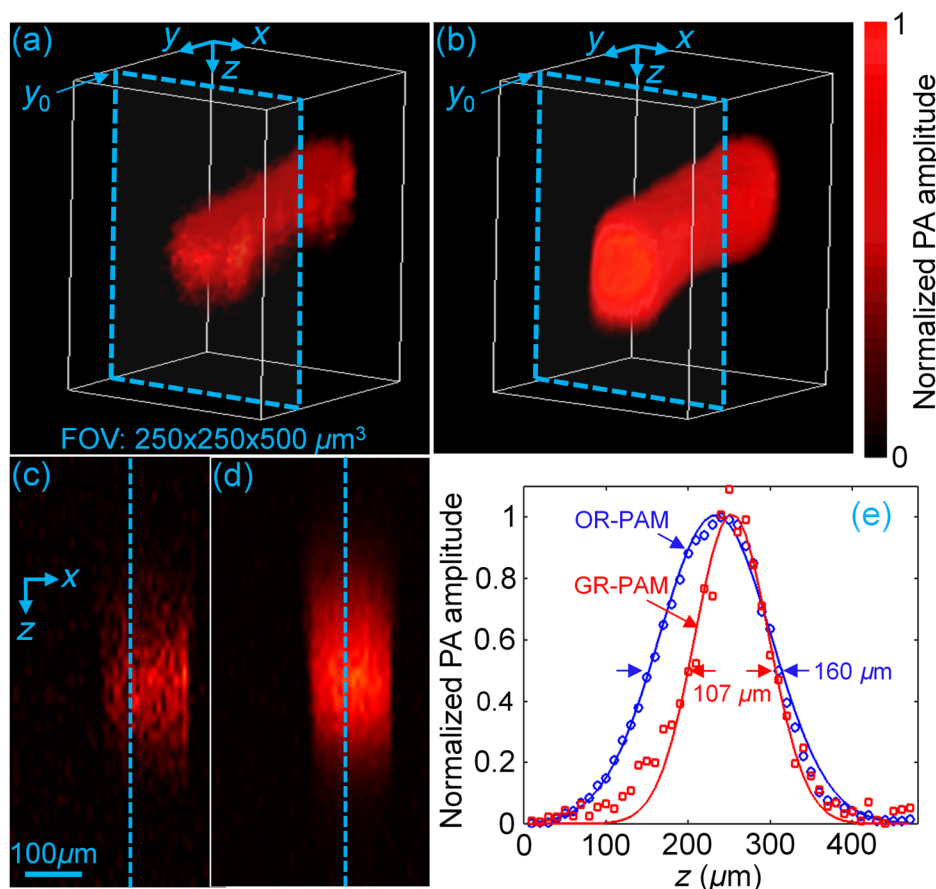


Fig. 4 (a) 3-D volume-rendered PA images of a blood-filled tube from GR-PAM and (b) 3-D-scanning conventional OR-PAM. (c) and (d) are B-scan images at the position y_0 , as indicated by the dashed box in the volume-rendered PA images in (a) and (b), respectively. (e) Profiles of the blood-filled tube along the dashed lines in (c) and (d).

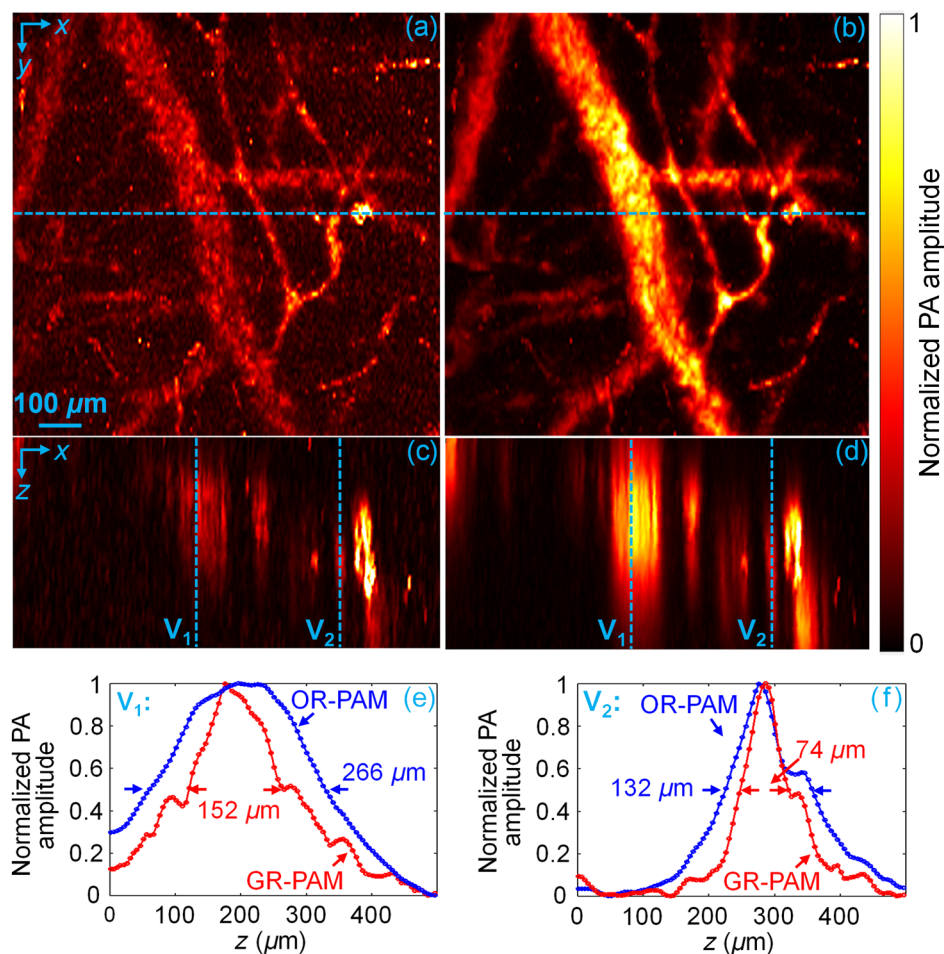


Fig. 5 (a) *In vivo* mouse brain images acquired by GR-PAM (b) and 3-D-scanning conventional OR-PAM. (c) B-scan images from GR-PAM and (d) 3-D-scanning conventional OR-PAM obtained by averaging five adjacent B-scans at the location indicated by the dashed lines in (a) and (b), respectively. (e) and (f) are the blood vessel profiles along the dashed lines in (c) and (d), respectively.

Figs. 5(c) and 5(d), the axial diameters of two blood vessels fitted from GR-PAM are ~ 150 and ~ 74 μm , much smaller than that measured by 3-D-scanning conventional OR-PAM (~ 266 and ~ 132 μm), as shown in Figs. 5(e) and 5(f). Currently, the wavelength of the laser used is 532 nm, and the maximum imaging depth for our GR-PAM is around 500 μm in our *in vivo* experiments. For deeper imaging, a red or near-infrared laser should be employed.²⁴

The acquisition time for a 3-D image with a volume of $200 \times 200 \times 100$ pixels is ~ 2.2 h. Over this period, minute brain motions, e.g., caused by cardiac pulsation, may degrade the image quality. This motion influence can potentially be reduced by using a laser with a high-repetition rate of 500 kHz,²³ which would reduce the acquisition time for the same 3-D image to 16 s.

5 Conclusion

We have demonstrated *in vivo* mouse brain imaging by GR-PAM for the first time. With a 25-MHz central-frequency UT, the measured axial resolution of GR-PAM in the phantom experiments was ~ 12.5 μm , sixfold better than that of 3-D-scanning conventional OR-PAM. The *in vivo* demonstration of GR-PAM shows the potential of this technique for label-free and

high-resolution anatomical and functional imaging of biological tissues.

Acknowledgments

The authors appreciate Professor James Ballard's help in editing this paper. The authors also thank Lidai Wang and Konstantin Maslov for discussions and technical help in the experiments. This work was supported in part by the National Institutes of Health, Grant Nos. DP1 EB016986 (NIH Director's Pioneer Award), R01 CA186567 (NIH Director's Transformative Research Award), R01 EB016963, and R01 CA159959. L.V.W. has a financial interest in Microphotoacoustics, Inc. which, however, did not support this work.

References

1. A. G. Bell, "On the production and reproduction of sound by light," *Am. J. Sci.* **s3-20**(118), 305–324 (1880).
2. L. V. Wang and S. Hu, "Photoacoustic tomography: in vivo imaging from organelles to organs," *Science* **335**(6075), 1458–1462 (2012).
3. S.-L. Chen, L. J. Guo, and X. Wang, "All-optical photoacoustic microscopy," *Photoacoustics* **3**(4), 143–150 (2015).
4. P. Beard, "Biomedical photoacoustic imaging," *Interface Focus* **1**(4), 602–631 (2011).

5. A. P. Jathoul et al., "Deep *in vivo* photoacoustic imaging of mammalian tissues using a tyrosinase-based genetic reporter," *Nat. Photonics* **9**, 239–246 (2015).
6. R. Cao et al., "Multispectral photoacoustic microscopy based on an optical-acoustic objective," *Photoacoustics* **3**(2), 55–59 (2015).
7. Y. Zhou et al., "Handheld photoacoustic microscopy to detect melanoma depth *in vivo*," *Opt. Lett.* **39**(16), 4731–4734 (2014).
8. C. Zhang et al., "In *in vivo* photoacoustic microscopy with 7.6- μm axial resolution using a commercial 125-MHz ultrasonic transducer," *J. Biomed. Opt.* **17**(11), 116016 (2012).
9. C. M. Daft, G. A. Briggs, and W. D. O'Brien, "Frequency dependence of tissue attenuation measured by acoustic microscopy," *J. Acoust. Soc. Am.* **85**(5), 2194–2201 (1989).
10. B. Dong et al., "Isometric multimodal photoacoustic microscopy based on optically transparent micro-ring ultrasonic detection," *Optica* **2**(2), 169–176 (2015).
11. C. Zhang et al., "Slow-sound photoacoustic microscopy," *Appl. Phys. Lett.* **102**(16), 163702 (2013).
12. L. Zhu et al., "Multiview optical resolution photoacoustic microscopy," *Optica* **1**(4), 217–222 (2014).
13. S. P. Mattison and B. E. Applegate, "Simplified method for ultra high-resolution photoacoustic microscopy via transient absorption," *Opt. Lett.* **39**(15), 4474–4477 (2014).
14. J. Yao et al., "Photoimprint photoacoustic microscopy for three-dimensional label-free subdiffraction imaging," *Phys. Rev. Lett.* **112**(1), 014302 (2014).
15. L. Wang, C. Zhang, and L. V. Wang, "Grueneisen relaxation photoacoustic microscopy," *Phys. Rev. Lett.* **113**(17), 174301 (2014).
16. J. Shi et al., "Bessel-beam Grueneisen relaxation photoacoustic microscopy with extended depth of field," *J. Biomed. Opt.* **20**(11), 116002 (2015).
17. J. Shah et al., "Photoacoustic imaging and temperature measurement for photothermal cancer therapy," *J. Biomed. Opt.* **13**(3), 034024 (2008).
18. D. Kobat, N. G. Horton, and C. Xu, "In *in vivo* two-photon microscopy to 1.6-mm depth in mouse cortex," *J. Biomed. Opt.* **16**(10), 106014 (2011).
19. Y. Yamaoka, M. Nambu, and T. Takamatsu, "Fine depth resolution of two-photon absorption-induced photoacoustic microscopy using low-frequency bandpass filtering," *Opt. Express* **19**(14), 13365–13377 (2011).
20. B. E. Urban et al., "Investigating femtosecond-laser-induced two-photon photoacoustic generation," *J. Biomed. Opt.* **19**(8), 085001 (2014).
21. L. V. Wang and H. Wu, *Biomedical Optics: Principles and Imaging*, John Wiley & Sons, Hoboken, New Jersey (2012).
22. R. L. Shelton and B. E. Applegate, "Off-axis photoacoustic microscopy," *IEEE Trans. Biomed. Eng.* **57**(8), 1835–1838 (2010).
23. J. Yao et al., "High-speed label-free functional photoacoustic microscopy of mouse brain in action," *Nat. Methods* **12**, 407–410 (2015).
24. P. Hai et al., "Near-infrared optical-resolution photoacoustic microscopy," *Opt. Lett.* **39**(17), 5192–5195 (2014).

Jun Ma received his BSc degree from Huazhong University of Science and Technology and a PhD from The Hong Kong Polytechnic University. Currently, he is working as a postdoctoral research associate at the Biomedical Engineering Department, Washington University in St. Louis. His research interests include optical acoustic and ultrasonic transducer, photoacoustic imaging, and their biomedical applications.

Junhui Shi received his BSc degree in chemical physics from the University of Science and Technology of China. Then, he continued to study chemistry and received his PhD from Princeton University, Princeton, New Jersey, USA. He was working on theoretical chemical dynamics and experimental nuclear magnetic resonance spectroscopy. Currently, he is working on photoacoustic imaging at the Biomedical Engineering Department, Washington University in St. Louis, Missouri, USA.

Pengfei Hai received his BS degree in biomedical engineering from Shanghai Jiao Tong University in 2012. He is currently a PhD candidate in biomedical engineering at the Washington University in St. Louis, under the supervision of Professor Lihong V. Wang. His research interests include the technical development and biomedical applications of photoacoustic imaging.

Yong Zhou is currently a graduate student in biomedical engineering at Washington University in St. Louis, under the supervision of Lihong V. Wang, Gene K. Beare distinguished professor. His research focuses on the development of photoacoustic imaging systems.

Lihong V. Wang is the Beare distinguished professor at Washington University. His book titled "Biomedical Optics" won the Goodman Award. He has published 420 journal articles with an h-index of 99 (>30,000 citations) and delivered 400 keynote/plenary/invited talks. His laboratory published first functional photoacoustic CT, three-dimensional photoacoustic microscopy, and compressed ultrafast photography. He serves as the editor-in-chief of the *Journal of Biomedical Optics*. He was awarded OSA's C.E.K. Mees Medal, NIH Director's Pioneer Award, and IEEE's Biomedical Engineering Award.